Cirrus spatial heterogeneity and ice crystal shape: Effects on remote sensing of cirrus optical thickness and effective crystal radius

H. Eichler,[1] K.S. Schmidt,[2] R. Buras,[3] M. Wendisch,[4] B. Mayer,[3,5] P. Pilewskie,[2] M.D. King,[2] L. Tian,[6] G. Heymsfield[6] S. Platnick[6]

H. Eichler, Institut für Physik der Atmosphäre (IPA), Johannes Gutenberg-Universität Mainz, Becherweg 21, Mainz, Deutschland. (eichlerh@uni-mainz.de)

K.S. Schmidt, Laboratory for Atmospheric and Space Physics, University of Colorado, Boulder, Colorado, USA. (Sebastian.Schmidt@lasp.colorado.edu)

R. Buras, Deutsches Zentrum für Luft- und Raumfahrt (DLR), Institut für Physik der Atmosphäre, Oberpfaffenhofen, Deutschland. (robert.buras@dlr.de)

M. Wendisch, Institut für Meteorologie (LIM), Universität Leipzig, Leipzig, Deutschland. (m.wendisch@uni-leipzig.de)

B. Mayer, Meteorologisches Institut der Ludwig-Maximilians-Universität, München, Deutschland. (bernhard.mayer@lmu.de)

P. Pilewskie, Laboratory for Atmospheric and Space Physics, University of Colorado, Boulder, Colorado, USA. (Peter.Pilewskie@lasp.colorado.edu)

M.D. King, Laboratory for Atmospheric and Space Physics, University of Colorado, Boulder, Colorado, USA. (Michael.King@lasp.colorado.edu)

L. Tian, NASA Goddard Space Flight Center, Greenbelt, Maryland, USA. (lin.tian-1@nasa.gov)

G. Heymsfield, NASA Goddard Space Flight Center, Greenbelt, Maryland, USA. (gerald.heymsfield@nasa.gov)

S. Platnick, NASA Goddard Space Flight Center, Greenbelt, Maryland, USA. (steven.platnick@nasa.gov)

Abstract.

We evaluate the relative importance of three-dimensional (3D) effects and ice crystal shape of spatially heterogeneous cirrus on the remote-sensing of optical thickness and effective crystal radius. In current ice cloud retrievals, the single scattering properties of ice crystals have to be assumed a-priori. Likewise, the effects of spatial cloud heterogeneity are ignored in current tech-

[1]Institut für Physik der Atmosphäre (IPA), Johannes Gutenberg-Universität Mainz, Deutschland.

[2]Laboratory for Atmospheric and Space Physics, University of Colorado, Boulder, Colorado, USA.

[3]Institut für Physik der Atmosphäre, DLR Oberpfaffenhofen, Deutschland.

[4]Institut für Meteorologie (LIM), Universität Leipzig, Leipzig, Deutschland.

[5]Meteorologisches Institut der Ludwig-Maximilians-Universität, München, Deutschland.

[6]NASA Goddard Space Flight Center, Greenbelt, Maryland, USA.

niques. Both simplifications introduce errors in the retrievals. Our study is based on 3D and independent pixel approximation (IPA) radiative transfer calculations. As model input we used a cloud case that was generated from data collected during the NASA Tropical Composition, Cloud, and Climate Coupling (TC^4) experiment. First, we calculated spectral upwelling radiance fields from the input cloud as they would be sensed by sensors from space or aircraft. We then retrieved the cirrus optical thickness and crystal effective radius that would be obtained in standard satellite techniques under the IPA assumption. The ratios between retrieved and the original fields are used as a metric for cloud heterogeneity effects on retrievals. Second, we used different single scattering properties (crystal shapes) in the retrievals than those used in the radiance calculations. In order to isolate ice crystal habit effects, the net horizontal photon transport was disabled in this part of the study. Here, the ratios between retrieved and original values of optical thickness and effective radius serve as metric for ice crystal habit effects. When comparing the two metrics, we found that locally, both can be of the same magnitude (up to 50 % over- and underestimation), with different dependencies on cirrus optical thickness, effective radius, and optical thickness variability. On domain average, shape effects bias the retrievals more strongly than 3D effects.

1. Introduction

Cirrus cloud remote sensing is different compared to the retrieval of microphysical properties of liquid water clouds not only because of the different genesis and thus different spatial distribution and dimensions of ice clouds, but also because they consist of ice crystals that are difficult to characterize in-situ or via remote sensing and to parameterize in radiative transfer calculations. The various crystal habits that occur in ice clouds add a degree of freedom to the retrievals because they have different single scattering properties for any given particle dimension. For this reason, a-priori assumptions about the single scattering properties of ensembles of ice crystals are made in most operational ice cloud retrievals. A similar, long-standing difficulty in liquid water and ice cloud remote sensing are spatial cloud heterogeneities over various scales. As yet, no practical solution has been proposed to resolve this issue, partly because these effects are so multi-facetted that there is no reasonable way to correct for them with a single method.

The classical *Nakajima and King* [1990] retrieval of cloud optical thickness (τ) and effective radius (R_{eff}) is based on measured cloud reflectance in two different wavelength channels, one in the visible to very near-infrared, where ice is practically non-absorbing, and one in the near-infrared range where ice crystals absorb solar radiation. Reflectance in the non-absorbing channel increases with τ and asymptotically approaches a value of about unity for optically thick clouds (the bidirectional reflectance can exceed unity). Similarly, reflectance in the near-infrared channel increases with τ; however, its limiting value is significantly less than unity, due to ice or liquid water absorption, and it decreases with particle size. Reflectance values in both channels are usually pre-calculated for a number of pairs of τ and R_{eff}, and observed values are matched with these lookup tables (LUT). In liquid water clouds, the two-dimensional reflectance space spanned by τ and R_{eff} can be determined with radiative transfer modelling in which the single scattering properties are determined by Mie theory because their constituents are spherical. For cirrus, in contrast, the retrieved microphysical products depend on the choice of shape of the crystal. Different crystal shapes exhibit different scattering phase functions and single scattering albedos as a function of size, and wavelength. Modelled single-scattering properties of non-spherical ice crystals are very diverse, [e.g., *Takano and Liou*, 1989; *Macke*, 1993] and result in substantially different lookup tables [*Eichler et al.*, 2009]. For example, the operational ice cloud procedures used for the Moderate Resolution Imaging Spectroradiometer (MODIS, *Platnick et al.* [2003]) Collection-5 retrievals [*King et al.*, 2006] were based on a different set of ice crystal optical properties [*Baum et al.*, 2005] than those for Collection-4. This change caused significant differences in the retrieved crystal effective radius of up to three μm [*Yang et al.*, 2007]. Evoked by the significant shape effects, methods were devised to detect ice crystal habit from non-polarized imager data [*McFarlane et al.*, 2005] and spectral reflectance measurements [*Francis et al.*, 1998].

Further complication is introduced by horizontal heterogeneities in the microphysical cloud properties. The well-known "cloud albedo-bias" (discussed mainly for liquid water clouds, [e.g., *Cahalan et al.*, 1994; *Barker*, 1996; *Carlin et al.*, 2002; *Oreopoulos et al.*, 2007], for example, is due to the non-linear convex (concave) dependence of reflectance in the non-absorbing (absorbing) wavelength on cloud τ (R_{eff}). It causes a systematic underestimation of τ or R_{eff} if cloud variability is not resolved within a pixel [e.g., *Marshak et al.*, 2006]. However, ever-increasing imager resolution can only partly remedy the problem: In the standard lookup table technique, the individual pixels are implicitly assumed to be independent of each other (independent pixel approximation, IPA). However, with increasing resolution, this assumption does not hold true because pixel-to-pixel horizontal transport of photons becomes important. This effect leads to so-called radiative smoothing or roughening. Smoothing was first discovered in the Landsat scale break (200 m were reported in a study by *Cahalan and Snider* [1989]). It leads to a suppression of variability on small scales. The characteristic length of horizontal photon transport is approximated by $\rho \approx h \cdot [(1-g)\tau]^{-1/2}$ [*Marshak et al.*, 1995] where h is the cloud geometrical thickness, and g is the asymmetry parameter. Less well-known is the fact that horizontal photon displacement is wavelength-dependent [*Platnick*, 2001; *Kassianov and Kogan*, 2002]. Photons that incur even weak absorption have considerably shorter horizontal path lengths. Apart from radiative smoothing, roughening is observed for special Sun-cloud geometries. For example, near-horizon Sun angles in conjunction with high cloud top variability lead to an increase in illumination contrasts and may cause overestimation of τ or R_{eff} [*Marshak et al.*, 2006]. Since the cloud albedo bias decreases with resolution while horizontal photon transport and illumination effects (smoothing and roughening) increase, it is generally assumed that optimum resolution is at around 1 km (*Zinner and Mayer* [2006], based on measured boundary-layer clouds). Vertical cloud structure is of special importance for R_{eff} retrievals *Platnick* [2000]. Multi-layer clouds can be detected with spectral imagery (*Wind et al.*, 2009, "Multilayer cloud detection with the MODIS near-infrared water vapor absorption band", submitted to *J. Appl. Meteor. Climatology*) but remain a challenge because they enhance cloud horizontal variability effects considerably, as we will show in this study.

It is widely accepted that neglecting either cirrus spatial variability or crystal shape leads to biases in remote-sensing products, however, their relative importance under different cloud conditions has not been studied systematically so far. It is unknown which effects dominate the error in standard retrievals, and which cloud parameters (τ, R_{eff}, cloud variability) determine the relative contributions. Such an assessment is the objective of this study. For a specific cloud case from the NASA Tropical Composition, Cloud, and Climate Coupling (TC^4) experiment (*Toon et al.*, 2009, "The planning and execution of TC^4", in this issue, submitted), we examine the impact of three-dimensional (3D) effects and ice crystal single scattering properties in heterogeneous cirrus clouds on remote-sensing products (τ and R_{eff}). This paper is the second in a series of three radiation-related publications within this TC^4 special issue. The first paper (*Kindel et al.*, 2009, "Observations and modeling of cirrus shortwave spectral albedo during the Tropical Composition, Cloud and Climate Coupling Experiment" in this issue, submitted) examines the consistency of ice cloud retrievals based on radiance and irradiance measurements. The third paper (*Schmidt et al.*, 2009, "Apparent and Real Absorption of Solar Spectral Irradiance in Heterogeneous Ice Clouds" in this issue, submitted) compares measured spectral ice cloud absorption with 3D radiation simulations.

Section 2.1 gives an overview of the modelling strategy applied in this paper. The analyzed cirrus cloud is introduced in Section 2.2. The cloud microphysical parameters have been generated from remote-sensing data of the MODIS Airborne Simulator (MAS) and Cloud Radar System (CRS) operated onboard the ER-2 aircraft. As explained in Section 2.2, the R_{eff} of the cloud field is vertically homogeneous while the cloud extinction varies with height. To assess the effects of cloud heterogeneities, we calculated spectral upwelling radiance fields along nadir track from the input cloud as they would be sensed from space or aircraft. We used the same ice cloud properties that are the basis for retrievals from MODIS and MAS. We then retrieved τ and R_{eff} that would be obtained from the standard MODIS/MAS algorithm under the IPA assumption (cf. Section 3.1). The ratios between the retrieved and the original fields of τ and R_{eff} serve as a metric for cloud heterogeneity effects on the retrievals. To estimate the error caused by inappropriate choices of ice crystal habits, we retrieved τ and R_{eff} assuming different crystal shapes (and thus different single scattering properties) than those used for calculating the radiance fields (cf. Section 3.2). In order to isolate ice crystal habit effects, the net horizontal photon transport was disabled in this part of the study (using the IPA assumption). Again the ratio between retrieved and input values of τ and R_{eff} serve as metric, here for ice crystal habit effects. We then compared the two types of ratios (heterogeneity and ice crystal shape effect). Sections 2.3 and 2.4 give an overview of the radiative transfer simulations and the lookup table method as well as associated uncertainties in the retrieval results. In Section 3.3, Ψ and Γ as metrics of the effects of 3D cloud structure and crystal habit are introduced, their magnitude and dependency on several cloud parameters is compared. The paper finishes with a summary and conclusions in Section 4.

2. Methodology

2.1. Strategy

In order to compare the impact of 3D effects and of crystal habits, we pursued the following strategy which is illustrated in Figure 1. Single scattering properties of various ice crystal parameterizations (ICP) from two studies were employed: *Baum et al.* [2005] give optical properties for a size-dependent mixture of crystal habits; *Key et al.* [2002]

provide single scattering properties for individual ice crystal habits (e.g., hexagonal plates (plt), solid columns (scl) and rough aggregates (agg)). The database of *Key et al.* [2002] is based on the one of *Yang et al.* [2000]. Subsequently, we refer to the different ICP as *Baum-mix*, *Key-plt*, *Key-scl*, and *Key-agg*. The strategy used in this work is as follows:

(a) Cloud generation: Build a 3D cloud field from MAS data (2D fields of τ and R_{eff}) and CRS data (vertical structure) obtained during the TC^4 experiment (cf. Section 2.2). Optical thickness and effective radius of this cloud are referred to as τ^{inp} and $R_{\mathrm{eff}}^{\mathrm{inp}}$.

(b) Consistency check: From this sample cloud, calculate upwelling radiances along nadir track $I_\lambda^{\uparrow,\mathrm{IPA}}$ (for wavelengths $\lambda = 870\,\mathrm{nm}$ and $\lambda = 2130\,\mathrm{nm}$, assuming *Baum-mix*) with the radiative transfer model MYSTIC (Monte Carlo code for the physically correct tracing of photons in cloudy atmospheres, *Mayer* [2009]) in independent pixel approximation (IPA) mode (cf. Section 2.3). Use these $I_\lambda^{\uparrow,\mathrm{IPA}}$ to retrieve back τ and R_{eff} with a pre-calculated lookup table (LUT) and compare those values to the input cloud values τ^{inp} and $R_{\mathrm{eff}}^{\mathrm{inp}}$ (cf. Section 2.5). The retrieved results should be consistent with the input cloud values since both, the MYSTIC-IPA calculations and the LUT, are based on *Baum-mix*.

(c) Impact of cloud heterogeneities (Γ ratios): Use MYSTIC in full 3D mode (see Section 2.3), along with *Baum-mix* to calculate upwelling radiances along nadir track ($I_\lambda^{\uparrow,\mathrm{3D}}$) at 500 m resolution as they would be measured by imaging radiometers. From these $I_\lambda^{\uparrow,\mathrm{3D}}$ derive τ^{3D} and $R_{\mathrm{eff}}^{\mathrm{3D}}$ using LUT with the same ice cloud optical properties as used in MYSTIC-3D (*Baum-mix*) to simulate a standard (e.g., MAS or MODIS) retrieval of τ and R_{eff}. Define ratios $\Gamma_\tau = \tau^{\mathrm{3D}}/\tau^{\mathrm{inp}}$ and $\Gamma_{R_{\mathrm{eff}}} = R_{\mathrm{eff}}^{\mathrm{3D}}/R_{\mathrm{eff}}^{\mathrm{inp}}$ as measures of 3D cloud structure effects.

(d) Impact of ice crystal shape (Ψ ratios): First, determine the crystal shape effect on upwelling radiance (illustrated in grey in Figure 1). Calculate $I_\lambda^{\uparrow,\mathrm{IPA}}$ for wavelengths $\lambda = 870\,\mathrm{nm}$ and $\lambda = 2130\,\mathrm{nm}$ using different ICP (*Baum-mix*, *Key-plt*, *Key-scl*, *Key-agg*) with MYSTIC-IPA (cf. Section 3.2.1). Secondly, from the *Baum-mix* calculated radiances, retrieve τ^{IPA} and $R_{\mathrm{eff}}^{\mathrm{IPA}}$ with *Key-plt*, *Key-scl*, *Key-agg* LUTs (cf. Section 3.2.2). Define ratios $\Psi_\tau = \tau^{\mathrm{IPA}}/\tau^{\mathrm{inp}}$ and $\Psi_{R_{\mathrm{eff}}} = R_{\mathrm{eff}}^{\mathrm{IPA}}/R_{\mathrm{eff}}^{\mathrm{inp}}$ as a measure of the ice crystal habit effect. IPA is used in order to better separate effects caused by crystal habit assumptions from cloud heterogeneity effects.

(e) Comparison: Assess the relative importance of 3D cloud structure (Γ) and crystal shape (Ψ) on the retrieved values, and examine the impact of cloud optical thickness, effective radius, and cloud variability on the two effects (cf. Section 3.3).

Several details about our methodology should be mentioned: First, the cloud field that serves as input to the MYSTIC-3D and MYSTIC-IPA radiative transfer calculations is already affected by 3D effects because it is based on data from an imaging radiometer (MAS). However, the results of our study are not dependent on closely we've matched the original cloud field; here we take the generated cloud as a realistic sample cloud. The choice of ICP (*Baum-mix*, *Key-plt*, *Key-scl*, *Key-agg*) does not represent all of the overall natural variability of crystal shapes and corresponding single scattering properties. Also, it should be mentioned that the *Baum et al.* [2005] parameterization uses an explicit scattering phase function (i.e., as function of the scattering angle), while the *Key et al.* [2002] parameterizations use a double Henyey-Greenstein parameterization for the scattering phase function. Hence, when analyzing Ψ ratios, it should be kept in mind that the deviation from unity does not solely result from the different ice crystal habits, but potentially could also stem from the different handling of the scattering phase function. However, the main differences between the different ICP are caused by differences in single scattering albedo and asymmetry parameter, both of which are well described by both *Baum-mix* and the *Key*-parameterizations. Secondary differences induced by particular features of the phase functions (which can not be reproduced by the double Henyey-Greenstein parameterization) are unlikely to change our results qualitatively, although minor quantitative changes can be expected.

2.2. Input Cloud

The data used for the generation of the 3D cirrus cloud was collected during the TC^4 experiment in Costa Rica in 2007. Among several aircraft, the high-altitude NASA ER-2 was employed. The aircraft was equipped with remote sensing instruments, such as the MODIS Airborne Simulator (MAS, *King et al.* [2004]), the Cloud Radar System (CRS, *Li et al.* [2004]), and the Solar Spectral Flux Radiometer (SSFR, *Pilewskie et al.* [2003]). Data from MAS and CRS were used to construct a 3D cloud based on the ER-2 flight leg from 15:20 to 15:35 UTC on July 17, 2007 (approximately 190 km long). The flight path was situated over the eastern Pacific approximately 550 km west of Columbia and 30 km south of Panama (around 5°N, 83°W). High level outflow cirrus downstream of a line of convective systems was probed. The ER-2 was flying above cloud top at 20 km towards the northwest and the solar incidence was from the northeast with a solar zenith angle of approximately 35°. The same cloud field was examined in a companion paper (*Schmidt et al.*, 2009, "Apparent and Real Absorption of Solar Spectral Irradiance in Heterogeneous Ice Clouds" in this issue, submitted) in the context of cloud absorption.

MAS retrieves horizontal fields of τ and R_{eff} from measurements of $I_\lambda^\uparrow$ at $\lambda = 870\,\text{nm}$ and $\lambda = 2130\,\text{nm}$ following the bispectral reflectance method introduced by *Nakajima and King* [1990] and described in detail for MODIS (and MAS) cloud products in *Platnick et al.* [2003]. In the derivation of MODIS and MAS ice cloud products, the single scattering properties of ice clouds are taken from the parameterization of *Baum et al.* [2005] which assumes a particle size dependent mixture of ice crystal habits consisting of droxtals, hexagonal plates, solid columns, hollow columns, aggregates, and spatial bullet rosettes. Optical properties are provided for particle sizes between 2-9500 μm and include scattering phase function and asymmetry parameter, extinction cross section, and single scattering albedo. For a more detailed description of this optical ice cloud parameterization refer to *Baum et al.* [2005].

The 2D field of τ retrieved from MAS gridded to 500 m resolution is shown in the upper panel of Figure 2. It covers an area of 192 km $\times$ 17.5 km (distance along flight track multiplied by MAS swath). The dashed line along y = 0 km represents the ER-2 flight track. Within the cloud scene, τ ranges between 5 and 45, with regions of high cloud extinction heterogeneity indicated by a high variability in τ. Cloud-free areas in the scene are displayed in white. The MAS-derived cloud top height along the nadir track varied between 8–12 km. It is represented by a black line in the vertical cross section of radar reflectivity from CRS in the lower panel of Figure 2. In addition to the outflow cirrus, some patches of low-level cloud between 0–3 km were present. The column-retrieved optical thickness comprises contributions from both low-level liquid and high-level ice clouds. For simplicity, both the low level and the high level clouds were treated as ice clouds in this modeling study.

The profile of radar reflectivity, Z, was used to derive approximate vertical profiles of ice water content ($IWC(z)$, in $\mathrm{g\,m^{-3}}$) along the flight track following *Liu and Illingworth* [2000]: $IWC = 0.137 \cdot Z^{0.64}$. For each vertical profile along the flight track, the column-integrated ice water path (IWP_{CRS}) was calculated. The IWP was also retrieved from MAS: $IWP_{\mathrm{MAS}} = 2/3 \cdot \rho_{ice} \cdot \tau \cdot R_{\mathrm{eff}}$ [*Stephens*, 1978], where ρ_{ice} is the density of ice (approximately 0.925 $\mathrm{g\,cm^{-3}}$). While the CRS profile was only measured along the center (nadir) track, MAS-derived IWP was available across the entire swath for each point along the track. In the model cloud, the IWC profiles were obtained through $IWC(z) = IWC_{\mathrm{CRS}} \cdot IWP_{\mathrm{MAS}}/IWP_{\mathrm{CRS}}$, with the assumption that the vertical distribution of ice water was constant across the MAS swath. The entire profile was shifted up or down corresponding to the cloud top height as retrieved by MAS. In lack of other information, the effective radius was set to $R_{\mathrm{eff}}(x, y, z) = R_{\mathrm{eff,MAS}}(x, y)$, that is, assumed constant throughout the entire cloud column. This is clearly a simplification because deeper down into the clouds, the crystal size distribution is fundamentally different from that near the top. Moreover, the R_{eff} in the underlying liquid water clouds is presumably much smaller. The MAS-derived R_{eff} is representative of the upper cloud layers [*Platnick*, 2000] where ice crystals are often smaller than in lower layers within the cirrus [e.g., *Francis et al.*, 1998; *Gayet et al.*, 2004]. Summarizing, all the cloud properties: IWC, τ, R_{eff}, and cloud top height were tied to MAS measurements; the CRS profiles were used to distribute the MAS-derived IWP in the vertical dimension, whereby another simplification consists in using the nadir-only CRS profiles for distributing IWP_{MAS} values vertically across the entire swath. Assumed ice crystal shapes were also set constant with height.

The generated 3D cloud (IWC, R_{eff}) was gridded to 500 m horizontal and 1000 m vertical resolution. For more information on the input cloud generation the reader is directed to the companion paper Part III (*Schmidt et al.*, 2009, "Apparent and Real Absorption of Solar Spectral Irradiance in Heterogeneous Ice Clouds" in this issue, submitted).

2.3. Radiative transfer modelling and retrieval method

All radiative calculations were done with the *libRadtran* (*lib*rary for *Rad*iative *tran*sfer) radiative transfer package by *Mayer and Kylling* [2005], using the different solvers and options. The generated 3D ice cloud field was used as input to the radiative transfer model (RTM). The radiative transfer calculations of $I_{\lambda}^{\uparrow}$ at 20 km altitude (the flight altitude of the ER-2) were performed with MYSTIC, the Monte Carlo code for the physically correct tracing of photons in cloudy atmospheres [*Emde and Mayer*, 2007; *Mayer*, 2009] which is embedded in *libRadtran*. In order to reduce computational time the simulations were performed in the backward Monte Carlo mode (i.e., tracing photons from the detector to the source; cf. *Mayer* [2009]) and using the bias-free "Variance Reduction Optimal Options Method" (VROOM, Buras, 2009, in preparation). 100.000 photons were traced for each wavelength and pixel along the nadir track, resulting in a standard deviation of 1.0–1.7 %. IPA calculations with MYSTIC (MYSTIC-IPA) were made by switching off net horizontal photon transport.

In the calculations, the single scattering properties of the crystal habit mix from *Baum et al.* [2005], and of the individual crystal habits (hexagonal plates, solid columns, and rough aggregates) from *Key et al.* [2002] were used. Both parameterize the shortwave bulk optical properties as function of R_{eff} and IWC. As mentioned in Section 2.1, they are referred to as *Baum-mix*, *Key-plt*, *Key-scl*, and *Key-agg*. As additional input parameters, the tropical standard atmospheric profile of temperature, pressure, relative humidity, and trace gas concentrations from *Anderson et al.* [1986] were used. Molecular absorption was parameterized by the LOWTRAN band model [*Pierluissi and Peng*, 1985] as adopted from SBDART [*Ricchiazzi et al.*, 1998]. The surface albedo of water was parameterized following *Cox and Munk* [1954] assuming a surface wind speed of $5\,\mathrm{m\,s^{-1}}$. Calculations were made at 870 nm (no cloud absorption, conservative scattering) and 2130 nm (ice crystals weakly absorbing, non-conservative scattering). The retrieval of τ and R_{eff} from the MYSTIC-3D and MYSTIC-IPA calculated radiances (leftward arrows in Figure 1) relies on bispectral lookup tables (LUT) as described by *Nakajima and King* [1990]. At 870 nm, the single scattering albedo of ice crystals is unity and the cloud top reflectance is mainly controlled by τ. At 2130 nm, absorption of solar radiation by ice depends strongly on R_{eff} and thus contains information on particle size. The LUTs were pre-calculated for pairs of cloud reflectance (870 nm and 2130 nm) using the DISORT2 algorithm [*Stamnes et al.*, 1988] which has been shown to agree with MYSTIC within better than 0.1 % for one-dimensional cases [*Mayer*, 2009]. Cloud top reflectance r is defined as the ratio of $\pi \cdot I_\lambda^{\uparrow}$ (at cloud top) divided by the downwelling irradiance incident at cloud top. For the solar geometry that prevailed during the flight leg, LUT calculations were performed for τ ranging from 0.1–70.1 in steps of 5 and R_{eff} ranging from 15–60 μm in steps of 5 μm. Therefore, *Baum-mix*, *Key-plt*, *Key-scl*, and *Key-agg* were used. For retrieving τ and R_{eff} from $I_\lambda^{\uparrow,\mathrm{3D}}$ and $I_\lambda^{\uparrow,\mathrm{IPA}}$ (assuming *Baum-mix*), the latter were first converted to reflectance pairs $r^{\mathrm{3D}}(870,\,2130)$ and $r^{\mathrm{IPA}}(870,\,2130)$. These reflectance values at 870 nm and 2130 nm were matched to the best-fitting pair of pre-calculated LUT reflectance pairs. The LUTs were interpolated linearly in order to obtain a finer resolution in τ and R_{eff}

space. The values of τ and R_{eff} as retrieved back from MYSTIC-3D calculated reflectance pairs $r^{3D}(870,\ 2130)$ are named τ^{3D} and R_{eff}^{3D}. They correspond to what remote sensing instruments would retrieve for the input cloud. Likewise, retrieved τ and R_{eff} values based on $I_{\lambda}^{\uparrow,\mathrm{IPA}}$ from the MYSTIC-IPA (*Baum-mix*) calculations are referred to as τ^{IPA}, and $R_{\mathrm{eff}}^{\mathrm{IPA}}$ (cf. Figure 1). These retrievals used LUTs based on *Key-plt*, *Key-scl*, and *Key-agg*. This method basically corresponds to a mapping of one LUT (*Baum-mix*) onto another (*Key-plt*, *Key-scl*, *Key-agg*) to determine the crystal shape effect, for each individual pixel.

2.4. Uncertainties of the method

When addressing the uncertainty of the retrieval results, several influences are considered. One part is the standard deviation of MYSTIC-IPA and MYSTIC 3D calculations and how they propagate into the retrieval results of τ and R_{eff}. This error component was examined by adding and subtracting the Monte Carlo standard deviations from the calculated reflectances. From these upper and lower limits of the calculated reflectance, the corresponding 1σ uncertainty range of τ and R_{eff} for each pixel was derived. Furthermore, uncertainties can arise from cloud top height differences in the input cloud and the fixed cloud top height of 11 km used for the LUT calculations. However, the influence of variations in cloud top height in the LUT calculations was tested and was found to be very small. Moreover, uncertainties in matching the reflectances of the model cloud to the best-fitting LUT reflectance pairs were determined. Therefore, the retrieval was made using MYSTIC-IPA $I_{\lambda}^{\uparrow}$ of a certain crystal habit and employing the corresponding LUT of the same habit. Retrieved τ and R_{eff} of all habits are expected to be alike and should reproduce the input cloud values (τ^{IPA} and $R_{\mathrm{eff}}^{\mathrm{IPA}}$) so the observed differences in the retrieval results are attributed to interpolation uncertainties. This procedure proves as validation of the used method and is described in detail in Section 2.5 for *Baum-mix*. The combined uncertainties of the mentioned potential error sources were determined. The standard deviations of the MYSTIC calculations influence the other mentioned uncertainties. However, Gaussian error combination gives an upper limit for the retrieval uncertainty and amount to 4 %, 2 %, 5 %, and 3 % for τ^{IPA}, $R_{\mathrm{eff}}^{\mathrm{IPA}}$, τ^{3D}, and $R_{\mathrm{eff}}^{\mathrm{3D}}$, respectively.

2.5. Consistency check

Calculations of $I_\lambda^\uparrow$ were made with MYSTIC in full 3D mode and in IPA mode for which net photon transport was disabled. This was done in order to use the exact same model for IPA and 3D calculations. To check that MYSTIC-IPA gives indeed the same results as the DISORT algorithm, IPA calculations with DISORT2 were made for each pixel. $I_\lambda^\uparrow$ determined with MYSTIC-IPA and DISORT2 agreed to within 0.5 % and 1.7 % (mean relative deviations at 870 nm and 2130 nm, respectively) assuring the number of photons used in the Monte Carlo simulations was adequate. Moreover, this agreement justifies using DISORT2 (instead of MYSTIC-IPA) in the determination of the LUT and the retrieval of τ^{IPA}, $R_{\mathrm{eff}}^{\mathrm{IPA}}$, τ^{3D}, and $R_{\mathrm{eff}}^{\mathrm{3D}}$. With MYSTIC-IPA calculations of $I_\lambda^\uparrow$ based on *Baum-mix*, retrieved τ^{IPA} and $R_{\mathrm{eff}}^{\mathrm{IPA}}$ with a LUT also based on *Baum-mix* should exactly reproduce the input cloud values. Actually the retrieved τ^{IPA} and $R_{\mathrm{eff}}^{\mathrm{IPA}}$ were almost equal to the original τ^{inp} and $R_{\mathrm{eff}}^{\mathrm{inp}}$ values, with only minor deviations (1 % in τ and 0.1 % in R_{eff} on average, see Figure 3).

3. Results

The retrieval results along the flight path in nadir direction are illustrated in the upper panels of Figure 3. Percentage deviations of the retrieved values from the input cloud values are shown in the lower panels. As obvious in the plot, the cloud field exhibited strong heterogeneities, with τ varying by a factor of 9 (τ = 5–45). Variations of R_{eff} were much smaller (up to a factor of 2) with R_{eff} ranging from 16 μm to 36 μm. Small R_{eff} were often observed during optically thinner parts of the cirrus while largest R_{eff} occured in optically thicker cloud regions.

3.1. 3D effects

Retrieved values (τ^{3D} and R_{eff}^{3D}) are influenced by horizontal as well as vertical cirrus inhomogeneities which can result in both over- and underestimation of τ and R_{eff}. Such effects are not captured by IPA calculations. In Figure 3a, the most pronounced feature in the time series of τ occurs at 110–120 km along the flight track where highest values of τ (30–45) were observed. The peak of 3D retrieved optical thickness (τ^{3D}, in green) is shifted with respect to the peak in the input cloud. The reason becomes obvious when looking at the off-nadir distribution of input optical thickness in the original cloud field (Figure 2). While on the flight track, the maximum occurs at 118 km, τ^{3D} along the flight track picks up contributions from cross-track pixels. Obviously, the high optical thickness areas at x≈105–115 km, y≈-5 km lead to a peak in τ^{3D} at x≈109 km. This is caused by *horizontal* photon transport from areas of high to low photon density (i.e., from bright to dark regions). In this case, this is equivalent to transport from high to low optical thickness areas.

Regions with a relatively thin cirrus layer in combination with patches of relatively thick low-level clouds (cf. Figure 2) are prone to strong *vertical* 3D effects: Photons reaching the low cloud are lost through the sides and eventually get absorbed by the dark ocean surface. This photon leakage results in an *underestimation* of τ as observed at distances of 42, 50, 85, 125–135 km along the flight track (cf. Figure 2 (upper panel), and Figure 4: underestimation of τ marked by dark red symbols). The effective radius is mostly *overestimated* along this specific flight track. Strong overestimation of the R_{eff} occurs mostly in optically thin regions (e.g., at 133–140 km along the flight track) or partly cloud-free areas (see Figure 2 (lower panel), strong overestimation marked by yellow symbols). In these areas radiation peneterates to the strongly absorbing sea-surface. However, upward scattering of photons at the low-level cloud can also cause increased reflectances at 2130 nm resulting in an *underestimation* of R_{eff} (e.g, at 89, 93, 123–125, 129–131 km along flight track). The strongest underestimations of R_{eff} are found in areas of thin (or broken) cirrus layers, with boundary layer clouds underneath. In the context of over- and underestimation of τ and R_{eff} by 3D calculations, the dependence of horizontal smoothing scale on wavelength as discussed in *Platnick* [2001] is important. There it was shown that the horizontal displacement of photons is considerably shorter at absorbing wavelengths. This leads to sharp peaks at which $R_{\mathrm{eff}}^{\mathrm{3D}}$ deviate from $R_{\mathrm{eff}}^{\mathrm{inp}}$. These peaks extend over only a few pixels because the horizontal transport of photons at 2130 nm is over short distances only (cf. Figure 3b). In contrast, τ^{3D} exhibit rather broad and smooth deviations from τ^{inp} (cf. Figure 3a). This is attributed to the long horizontal smoothing scales at 870 nm, the wavelength used for the determination of τ^{3D}. The different horizontal path lengths at 870 nm and 2130 nm cause different reflectance enhancement factors in the 3D calculations so that under- or overestimations of τ^{inp} and $R_{\mathrm{eff}}^{\mathrm{inp}}$ have different magnitudes and spatial extents.

In Figure 4, τ^{3D} and R_{eff}^{3D} (assuming *Baum-mix*) are plotted versus τ^{inp} and $R_{\text{eff}}^{\text{inp}}$. Strong under- and overestimation of the original values are marked with dark red and yellow symbols, respectively. The thresholds in Figure 4 are chosen for illustration of those regions at which under- and overestimations occur in Figure 2 and Figure 3 (highlighted by marks with the same color code). Figure 4a shows that for the observed cloud scene, remote-sensing instruments with 500 m spatial resolution (which measure $I_{\lambda}^{\uparrow,3D}$ influenced by cloud 3D effects) would mostly underestimate the true τ by more than 20 %. At the same time (cf. Figure 4b and Figure 3b), they would often overestimate R_{eff} by about 3–15 %. Averaged over the flight leg from 15.5–182.0 km, the original optical thickness, τ^{inp} is 16, and the retrieved value, τ^{3D} is 14 (12 % underestimation). Similarly, averaged $R_{\text{eff}}^{\text{inp}} = 27\,\mu$m, and averaged $R_{\text{eff}}^{3D} = 28\,\mu$m (4 % overestimation). The underestimation of τ and overestimation of R_{eff} by IPA retrievals based on remotely sensed $I_{\lambda}^{\uparrow,3D}$ was also found by *Marshak et al.* [2006] who attributed it to shadowing effects in boundary layer clouds. In our case, shadowing effects did not play a significant role in producing the same biases. The effects of cloud illumination and cloud top structure were of minor importance in our case, partly because of the near-zenith sun position, and partly because of the flat cloud top topography, compared to the liquid water clouds studied by *Marshak et al.* [2006].

3.2. Crystal shape effects

3.2.1. Impact on reflected radiances

In order to understand the crystal shape effects on retrieved cloud microphysical properties, first the crystal shape effect on $I_{\lambda}^{\uparrow,\text{IPA}}$ is discussed, using MYSTIC-IPA calculations at 870 nm and 2130 nm wavelength and assuming different ICP. First, the dependence of $I_{\lambda}^{\uparrow,\text{IPA}}$ on τ^{inp} was examined. The non-linear increase of $I_{870}^{\uparrow,\text{IPA}}$ (or reflectance r_{870}) with increasing τ^{inp} is illustrated in Figure 5a. Assuming *Key-scl* or *Key-agg* leads to higher values of $I_{870}^{\uparrow,\text{IPA}}$ than assuming *Baum-mix*. The *Key-plt* assumption generally results in lower values of $I_{870}^{\uparrow,\text{IPA}}$. Deviations from the logarithmic dependence of $I_{870}^{\uparrow,\text{IPA}}$ with increasing τ^{inp} are obvious for $\tau^{\text{inp}}<12$ for *Key-plt*. The variability of the reflectance for a given τ^{inp} value stems from the variable R_{eff}.

Figure 6a shows the ratio of $I_{870}^{\uparrow,\text{IPA}}(Key)$ and $I_{870}^{\uparrow,\text{IPA}}(Baum\text{-}mix)$. At non-absorbing wavelengths (i.e., 870 nm) the differences between various ICP become less significant with increasing τ because cloud reflectance becomes saturated and is approaching unity at $\tau^{\text{inp}} > 45$. Multiple scattering washes out the differences in the single-scattering properties of the various crystal habits. The same finding of diminishing crystal shape effects with increasing τ was made by *Wendisch et al.* [2005] for irradiances at scattering wavelengths.

Figure 5b shows $I_{\lambda}^{\uparrow,\text{IPA}}$ at the absorbing wavelength (2130 nm) versus τ^{inp}. $I_{2130}^{\uparrow,\text{IPA}}$ determined using *Key-scl* or *Key-agg* lead to higher values of $I_{2130}^{\uparrow,\text{IPA}}$ compared to *Baum-mix* and *Key-plt*. The fact that $I_{2130}^{\uparrow,\text{IPA}}$ using the different single habits of the *Key*-ICP are generally higher than $I_{2130}^{\uparrow,\text{IPA}}$ of the *Baum-mix* can be explained as follows: The *Baum-mix* does not only consist of plates, columns, and aggregates but also of droxtals (small crystals) and bullet-rosettes (large crystals) which are not considered separately here. $I_{2130}^{\uparrow,\text{IPA}}$ (or reflectance r_{2130}) are found to saturate at a crystal shape-dependent upper limit. This limit is reached at smaller optical depths than for non-absorbing wavelengths (at around $\tau^{\text{inp}} \approx 12$). Due to absorption, the limit is lower than unity. Its value depends only on the single scattering albedo which in turn depends on the crystal habit. That means from $\tau^{\text{inp}} \approx 12$ onward, a constant $I_{2130}^{\uparrow,\text{IPA}}$ (or r_{2130}) value which is dependent on crystal habit is reached (cf. Figure 5b).

This is also shown in Figure 6b, where the ratio of $I_{2130}^{\uparrow,\mathrm{IPA}}(Key)$ and $I_{2130}^{\uparrow,\mathrm{IPA}}(Baum\text{-}mix)$ is shown. Observed shape-induced differences in $I_{2130}^{\uparrow,\mathrm{IPA}}$ were independent of τ^{inp} for $\tau^{\mathrm{inp}} > 12$. *Wendisch et al.* [2005] found that for irradiances at absorbing wavelengths the shape effects increased with increasing τ. However, this was for clouds with $\tau < 7$ only. As shown, in the limit of larger τ, the reflectance also becomes saturated and approaches an upper limit.

3.2.2. Impact on retrieved microphysical cirrus properties

Figure 7a and 7b show the MYSTIC-IPA based τ^{IPA} and $R_{\mathrm{eff}}^{\mathrm{IPA}}$ values as a function of the values in the original input file, for all pixels along the flight track. When using the LUT based on *Baum-mix*, one retrieves the same values (black symbols on the 1:1 line) because this is the same ICP as used in the MYSTIC-IPA calculations. When using other ICP for the generation of LUT such as *Key-plt*, *Key-scl*, *Key-agg*, the retrieval results differ from the values in the input cloud. Highest values of τ^{IPA} are retrieved assuming *Key-plt* while using *Key-scl* and *Key-agg* results in smaller values of τ^{IPA} (always compared to using *Baum-mix*). Similar findings were reported by *McFarlane et al.* [e.g., 2005]; *Eichler et al.* [e.g., 2009]. The assumption of *Key-scl* or *Key-agg* leads to larger values of $R_{\mathrm{eff}}^{\mathrm{IPA}}$ whereas using the LUT based on *Key-plt* results in $R_{\mathrm{eff}}^{\mathrm{IPA}}$ similar to the ones retrieved using *Baum-mix*.

3.3. 3D versus shape effects

In this section, the relative importance of the 3D cloud structure and ice crystal habit is assessed. For that reason, measures of 3D cloud structure (Γ) and ice crystal habit (Ψ) are introduced.

Γ_τ and $\Gamma_{R_{\rm eff}}$ are defined as ratio between the LUT-retrieval results based on MYSTIC-3D calculated radiances and the original values of the input cloud. They serve as measure of 3D effects:

$$\Gamma_\tau = \frac{\tau^{\rm 3D}}{\tau^{\rm inp}} \; and \; \Gamma_{R_{\rm eff}} = \frac{R_{\rm eff}^{\rm 3D}}{R_{\rm eff}^{\rm inp}}. \tag{1}$$

Ψ_τ and $\Psi_{R_{\rm eff}}$ are defined as ratio between the retrieval results based on MYSTIC-IPA calculations and the original values of the input cloud:

$$\Psi_\tau = \frac{\tau^{\rm IPA}}{\tau^{\rm inp}} \; and \; \Psi_{R_{\rm eff}} = \frac{R_{\rm eff}^{\rm IPA}}{R_{\rm eff}^{\rm inp}}. \tag{2}$$

Ψ is a measure of the effects of crystal habit on the retrieval results. While the MYSTIC-IPA calculations (τ, $R_{\rm eff} \rightarrow I_\lambda^\uparrow$) are based on *Baum-mix*, the LUT-based retrievals ($I_\lambda^\uparrow \rightarrow \tau$, $R_{\rm eff}$) use *Key-scl*, *Key-agg*, and *Key-plt*. *Baum-mix* is also used in the retrievals to verify that it reproduces the same values for τ and $R_{\rm eff}$ as those in the original cloud field. For simplicity, the labels for the individual habits are omitted on the Ψ symbols. *Baum-mix* is chosen as reference habit because it is used in MODIS Collection-5 standard ice cloud retrievals.

Figure 8a shows Γ_τ and Ψ_τ as function of $\tau^{\rm inp}$. The black crosses mark 3D effects and the colored symbols the shape effects. Both have roughly the same magnitude with a maximum over- and underestimation of τ of 50 %. The shape-ratios (Ψ_τ) are constant with $\tau^{\rm inp}$: Using *Key-plt* for the retrievals leads to an overestimation of $\tau^{\rm inp}$ by nearly 50 %; using *Key-scl* or *Key-agg* results in an underestimation by approximately 20 % (in agreement with *Eichler et al.* [2009]). In contrast, Γ_τ decreases from values around unity (range from 0.6–1.4) at zero optical thickness to about 0.6 for $\tau^{\mathrm{inp}} = 40$. The growing extent of underestimation of τ with increasing τ can be viewed as direct consequence of radiative smoothing of the reflectance fields. In the absence of shadows, photons are effectively redistributed from areas of maximum optical thickness to the surroundings. Since LUT-techniques do not correct for this net horizontal transport, optical thickness is underestimated in optically thick regions, and overestimated elsewhere. In clear-sky or optically very thin areas ($\tau < 3$), photons may even get absorbed at the surface. As shown in Section 3.1, over- and underestimation do not cancel each other out, and τ is underestimated by 12 % on domain-average. Part of this net underestimation may be because of surface absorption. For small τ, under- and overestimation of τ seems to be equally likely (40 %). Linear regression shows that $\Gamma_\tau \rightarrow 1$ for $\tau^{\mathrm{inp}} \rightarrow 0$. Potentially, the dependence of Γ_τ on τ (slope) could be a useful indicator for the impact of cloud heterogeneity on retrievals.

The dependence of $\Gamma_{R_{\mathrm{eff}}}$ and $\Psi_{R_{\mathrm{eff}}}$ on $R_{\mathrm{eff}}^{\mathrm{inp}}$ is shown in Figure 8b. $\Gamma_{R_{\mathrm{eff}}}$ generally ranges between 0.9–1.1. Larger values (>1.1, more than 10 % overestimation) were observed when low-level clouds were present. It slightly decreases with increasing $R_{\mathrm{eff}}^{\mathrm{inp}}$. On average, $\Gamma_{R_{\mathrm{eff}}} \approx 1.04$ (4 % overestimation). Shape-related biases in $R_{\mathrm{eff}}^{\mathrm{inp}}$ can amount to 60 % for largest observed crystals ($R_{\mathrm{eff}} = 35\,\mu$m). R_{eff} strongly depends on the chosen ICP: When using *Key-agg* in the retrieval, R_{eff} increases from 1.2 to 1.6 with increasing $R_{\mathrm{eff}}^{\mathrm{inp}}$. For *Key-scl*, $R_{\mathrm{eff}}^{\mathrm{inp}}$ has a constant value of 1.3 while it decreases from 1.15 to 1 for *Key-plt*. The different functional dependence of R_{eff} for *Key-agg*, *Key-scl*, and *Key-plt* can be ascribed to a different dependence of the single scattering albedo (SSA) at 2130 nm on R_{eff} for the different crystal habits. The magnitude of the shape-related bias is comparable to that of 3D effects only for *Key-plt*, and exceeds it by far for *Key-agg* and *Key-scl*. In our case, the choice of habit has a much larger impact on size retrievals than 3D effects. Note that the largest habit-related bias in τ is observed for *Key-plt* (red dots), while *Key-agg* (blue dots) introduce the largest bias for R_{eff}. The reason is that at the non-absorbing wavelength, *Key-plt* exhibits a strong forward peak in the scattering phase function, thus leading to the most pronounced shape effect in the retrieval of τ. In contrast, at 2130 nm the SSA of *Key-agg* or *Key-scl* for a given $R_{\mathrm{eff}}^{\mathrm{inp}}$ differ from that of the *Baum-mix*, resulting in high $\Psi_{R_{\mathrm{eff}}}$. The SSA of *Key-plt* is similar to that of *Baum-mix* thus leading to a good agreement of R_{eff}.

In Figure 8c, $\Gamma_{R_{\mathrm{eff}}}$ and $\Psi_{R_{\mathrm{eff}}}$ are displayed as function of τ^{inp}. As described in Section 3.1, multi-layer effects with optically thin cirrus and patches of low-level clouds are responsible for extremely high (>1.1) or low (<0.9) values of $\Gamma_{R_{\mathrm{eff}}}$. Horizontal inhomogeneities result in $0.9 < \Gamma_{R_{\mathrm{eff}}} < 1.1$. The linear fit of $\Gamma_{R_{\mathrm{eff}}}$ in Figure 8c shows that 3D cloud effects on R_{eff} generally cause an overestimation of R_{eff} with increasing τ^{inp}. $\Gamma_{R_{\mathrm{eff}}} \sim 1$ is extrapolated for $\tau^{\mathrm{inp}} \to 0$. For $\tau^{\mathrm{inp}} \approx 40$, $\Gamma_{R_{\mathrm{eff}}}$ reaches about 1.08. The $\Psi_{R_{\mathrm{eff}}}$ are independent of τ for $\tau^{\mathrm{inp}} > 12$, and larger in magnitude than $\Gamma_{R_{\mathrm{eff}}}$ (up to 1.6 for *Key-agg*). For $\tau^{\mathrm{inp}} < 12$, $\Psi_{R_{\mathrm{eff}}}(\tau)$ have about the same magnitude as $\Gamma_{R_{\mathrm{eff}}}(\tau)$. They increase (for *Key-scl* and *Key-agg*) or decrease (for *Key-plt*) for $5 < \tau^{\mathrm{inp}} < 12$. In optically thick regions of the cloud, the retrieval of R_{eff} is more influenced by crystal habit effects than cloud heterogeneity effects.

Finally, we tested if a systematic dependence of $\Gamma_{R_{\mathrm{eff}}}$ or Γ_τ on the cloud optical thickness variability can be found. The cloud optical thickness variability was parameterized by the standard deviation of τ^{inp} within a circle of 1 km radius around each individual pixel. While Γ_τ did not show any systematic trend, $\Gamma_{R_{\text{eff}}}$ is slightly increasing with cloud variability. This is shown in Figure 8d. $\Gamma_{R_{\text{eff}}} \sim 1$ is extrapolated for a cloud with zero optical thickness variability within a 1 km circle. The finding that 3D retrieval biases do not (or only insignificantly) depend on the magnitude of cloud optical thickness variability is somewhat surprising. Instead, we found that 3D retrieval biases depend on the values of τ and R_{eff} themselves.

4. Summary and Conclusions

In this study, the relative impact of single scattering properties and cloud variability in ice clouds on remote-sensing products (cirrus optical thickness τ and effective crystal radius R_{eff}) was examined. The work is based on a cloud field that was encountered during the NASA TC^4 experiment. From MODIS Airborne Simulator and Cloud Radar System data a cloud field for input to 3D radiative transfer calculations was constructed. In this cloud field of 500 m horizontal resolution, extinction varies with height albeit the effective radius is vertically homogeneous. The radiative transfer model was run in full 3D and IPA mode and employed the same ice crystal scattering properties (*Baum-mix*) that are used in MODIS Collection-5 retrievals. Upwelling radiances along the flight track of the ER-2 for two wavelengths, 870 nm and 2130 nm were calculated. Then a retrieval process was simulated: the bispectral radiance values were mapped back onto values of cirrus optical thickness and effective crystal radius, as is usually done in standard lookup table (LUT) techniques. The LUTs were pre-calculated with the DISORT2 1D radiative transfer model. Different LUTs were made for different crystal habits: a mixture of particle habits (*Baum-mix*); hexagonal plates, solid columns, and rough aggregates (*Key-plt*, *Key-scl*, *Key-agg*). The full 3D calculations simulated the radiance field along nadir track that a satellite imager would detect for the given cloud distribution. In order to estimate the magnitude of 3D effects, the resulting LUT-based retrievals were compared to the original input cloud field. Γ was defined as ratio between those retrieval results and the input cloud optical thickness τ^{inp} or effective radius $R_{\mathrm{eff}}^{\mathrm{inp}}$. To cancel out shape effects, the retrievals were based on the same crystal scattering properties as in the 3D calculations (*Baum-mix*). In the second step, the shape effects were examined, and all four pre-calculated LUTs were used to retrieve optical thickness and effective radius. In order to single out the shape effects, net horizontal photon transport was disabled in the radiance calculations and IPA mode 3D model runs were used. The ratio between the retrievals and the original input values, Ψ, was introduced as measure of the ice crystal habit effect.

Both Γ and Ψ were analyzed as function of τ^{inp}, $R_{\mathrm{eff}}^{\mathrm{inp}}$, and cloud variability. On the domain average, we found that cirrus optical thickness is underestimated by 12 %, and effective crystal radius is overestimated by 4 %, due to 3D effects. In comparison, shape effects may bias the retrieval much more strongly: Assuming plates rather than the standard *Baum-mix* in the retrievals leads to an overestimation of optical thickness of 50 %; the effective radius is overestimated by 60 % when assuming aggregates rather than the standard.

The shape-induced biases in optical thickness are constant in thick and thin cloud areas. In contrast, the 3D bias in τ ranges from 60 % underestimation to 40 % overestimation locally. Large τ values are generally underestimated. Both under- and overestimation occur in optically thin areas. The shape-induced effective radius biases depend strongly on ice particle size itself. While for small crystals, *Key-plt*, *Key-scl*, and *Key-agg* are moderately biased positive with respect to *Baum-mix* (15–25 %), they overestimate the effective radius by up to 60 % for large crystal sizes. By comparison, 3D effects cause underestimations of 10 % to overestimations of 20 %. In areas with pronounced multi-layer structure, the effective crystal radius is overestimated by up to 30 %.

Acknowledgments. Heike Eichler was financed by the Collaborative Research Center 641 TROPICE "The Tropospheric Ice Phase". RTE-calculations were made at DLR, Oberpfaffenhofen, Germany. Sebastian Schmidt and Michael King were funded under the NASA TC4 project (project number NNX07AL12G and NNX08AR39G, respectively), as were the deployment of MAS and CRS onboard the NASA ER-2 aircraft. Steven Platnick and Paul Newman (NASA Goddard) were ER-2 flight scientists on the 17th of July, 2007. The NASA ESPO team managed the project logistics in Costa Rica and elsewhere.

BIBLIOGRAPHY

References

Anderson, G., S. Clough, F. Kneizys, J. Chetwynd, and E. Shettle (1986), AFGL Atmospheric Constituent Profiles (0-120 km), *Tech. Rep. AFGL-TR-86-0110*, AFGL (OPI), Hanscom AFB, MA 01736.

Barker, H. (1996), A parameterization for computing grid-averaged solar fluxes for inhomogeneous marine boundary layer clouds. Part I: Methodology and homogeneous biases, *J. Atmos. Sci.*, *53*(16), 2289–2303.

Baum, B. A., P. Yang, A. J. Heymsfield, S. Platnick, M. D. King, Y. X. Hu, and S. T. Bedka (2005), Bulk scattering properties for the remote sensing of ice clouds. part ii: Narrowband models, *J. Appl. Meteor.*, *44*(12), 1896–1911.

Cahalan, R., and J. Snider (1989), Marine stratocumulus structure, *Remote Sens. Environ.*, *28*, 95–107.

Cahalan, R., W. Ridgway, W. Wiscombe, and T. Bell (1994), The albedo of fractal stratocumulus clouds, *J. Atmos. Sci.*, *51*, 2434–2455.

Carlin, B., Q. Fu, U. Lohmann, G. Mace, K. Sassen, and J. Comstock (2002), High-cloud horizontal inhomogeneity and solar albedo bias, *J. Climate*, *15*, 2321–2339.

Cox, C., and W. Munk (1954), Measurement of the roughness of the sea surface from photographs of the sun's glitter, *Journal of the Optical Society of America*, *44*(11), 838–850.

Eichler, H., A. Ehrlich, M. Wendisch, G. Mioche, J.-F. Gayet, M. Wirth, C. Emde, and A. Minikin (2009), Influence of ice crystal shape on retrieval of cirrus optical thickness and effective radius: A case study, *Journal of Geophysical Research*, *accepted*.

Emde, C., and B. Mayer (2007), Simulation of solar radiation during a total solar eclipse: A challenge for radiative transfer., *Atmos.Chem.Phys.*, *7*, 2259–2270.

Francis, P., P. Hignett, and A. Macke (1998), The retrieval of cirrus cloud properties from aircraft multi-spectral reflectance measurements during EUCREX '93, *Q.J.R. Meteorol. Soc.*, *124*, 1273–1291.

Gayet, J. F., J. Ovarlez, V. Shcherbakov, J. Strom, U. Schumann, A. Minikin, F. Auriol, A. Petzold, and M. Monier (2004), Cirrus cloud microphysical and optical properties at southern and northern midlatitudes during the INCA experiment, *J. Geophys. Res.*, *109*(D20), Art. No. D20,206.

Kassianov, E., and Y. Kogan (2002), Spectral dependence of radiative horizontal transport in stratocumulus clouds and its effect on near-IR absorption, *J. Geophys. Res.*, *107*(D23), doi:10.1029/2002JD002,103.

Key, J. R., P. Yang, B. A. Baum, and S. L. Nasiri (2002), Parameterization of shortwave ice cloud optical properties for various particle habits, *J. Geophys. Res.*, *107*(D13), Art. No. 4181.

King, M., P. Platnick, P. Hubanks, G. Arnold, E. Moody, G. Wind, and B. Wind (2006), Collection 005 Change Summary for the MODIS Cloud Optical Property Algorithm., http://modis-atmos.gsfc.nasa.gov/C005_Changes/C005_CloudOpticalProperties_ver311.pdf.

King, M. D., S. Platnick, P. Yang, G. T. Arnold, M. A. Gray, J. C. Riedi, S. A. Ackerman, and K. N. Liou (2004), Remote sensing of liquid water and ice cloud optical thickness and effective radius in the Arctic: Application of airborne multispectral MAS data, *J. Atmos. Oceanic Technol.*, *21*(6), 857–875.

Li, L., G. Heymsfield, P. Racette, L. Tian, and E. Zenker (2004), A 94 GHz cloud radar system on a NASA high-altitude ER-2 aircraft, *J. Atmos. Ocean Technol.*, *21*, 1378–1388.

Liu, C.-L., and A. Illingworth (2000), Toward more accurate retrievals of ice water content from radar measurements of clouds, *J. Appl. Meteorol.*, *39*, 1130–1146.

Macke, A. (1993), Scattering of light by polyhedral ice crystals, *Appl. Opt.*, *32*(15), 2780–2788.

Marshak, A., A. Davis, W. Wiscombe, and R. Cahalan (1995), Radiative smoothing in fractal clouds, *J. Geophys. Res.*, *100*(D12), 26,247–26,261.

Marshak, A., S. Platnick, T. Varnai, G. Y. Wen, and R. F. Cahalan (2006), Impact of three-dimensional radiative effects on satellite retrievals of cloud droplet sizes, *Journal*

Of Geophysical Research-Atmospheres, *111*(D9).

Mayer, B. (2009), Radiative transfer in the cloudy atmosphere, *The European Physical Journal Conferences*, *1*, 75–99.

Mayer, B., and A. Kylling (2005), Technical note: The libRadtran software package for radiative transfer calculations - description and examples of use, *Atmos. Chem. Phys.*, *5*, 1.855–1.877.

McFarlane, S. A., R. T. Marchand, and T. P. Ackerman (2005), Retrieval of cloud phase and crystal habit from Multiangle Imaging Spectroradiometer (MISR) and Moderate Resolution Imaging Spectroradiometer (MODIS) data, *J. Geophys. Res.*, *110*(D14), Art. No. D14,201.

Nakajima, T., and M. King (1990), Determination of the optical thickness and effective particle radius of clouds from reflected solar radiation measurements. Part I: Theory, *J. Atmos. Sci.*, *47*, 1878–1893.

Oreopoulos, L., R. F. Cahalan, and S. Platnick (2007), The plane-parallel albedo bias of liquid clouds from modis observations, *J. Climate*, *20*(20), 5114–5125.

Pierluissi, J., and G.-S. Peng (1985), New molecular transmission band models for LOWTRAN, *Optical Engineering*, *24*(3), 541–547.

Pilewskie, P., J. Pommier, R. Bergstrom, W. Gore, S. Howard, M. Rabbette, B. Schmid, P. V. Hobbs, and S. C. Tsay (2003), Solar spectral radiative forcing during the Southern African Regional Science Initiative, *J. Geophys. Res.*, *108*, doi:10.1029/2002JD002,411.

Platnick, S. (2000), Vertical photon transport in cloud remote sensing problems, *J. Geophys. Res.*, *105*(D18), 22,919–22,935.

Platnick, S. (2001), Approximations for horizontal photon transport in cloud remote sensing problems, *J. Quant. Spectrosc. Ra.*, *68*, 75–99.

Platnick, S., M. King, S. Ackerman, W. Menzel, B. Baum, J. Riedi, and R. Frey (2003), The MODIS cloud products: Algorithms and examples from TERRA, *IEEE Trans. Geosci. Remote Sens.*, *41*, 459–473.

Ricchiazzi, P., S. Yang, C. Gautier, and D. Sowle (1998), SBDART: A research and teaching software tool for plane-parallel radiative transfer in the Earth's atmosphere, *Bull. Amer. Meteorol. Soc.*, *79*, 2101–2114.

Stamnes, K., S. Tsay, W. Wiscombe, and K. Jayaweera (1988), A numerically stable algorithm for discrete-ordinate-method radiative transfer in multiple scattering and emitting layered media, *Appl. Opt.*, *27*(12), 2502–2509.

Stephens, G. (1978), Radiation profiles in extended water clouds. II: Parameterization schemes, *J. Atmos. Sci.*, *35*, 2123–2132.

Takano, Y., and K.-N. Liou (1989), Solar radiative transfer in cirrus clouds. Part I: Single-scattering and optical properties of hexagonal ice crystals, *J. Atmos. Sci.*, *46*, 1–19.

Wendisch, M., P. Pilewskie, J. Pommier, S. Howard, P. Yang, A. J. Heymsfield, C. G. Schmitt, D. Baumgardner, and B. Mayer (2005), Impact of cirrus crystal shape on solar spectral irradiance: A case study for subtropical cirrus, *J. Geophys. Res.*, *110*(D3), Art. No. D03,202.

Yang, P., K. N. Liou, K. Wyser, and D. Mitchell (2000), Parameterization of the scattering and absorption properties of individual ice crystals, *J. Geophys. Res.*, *105*(D4), 4.699–4.718.

Yang, P., L. Zhang, G. Hong, S. L. Nasiri, B. A. Baum, H. L. Huang, M. D. King, and S. Platnick (2007), Differences between collection 4 and 5 modis ice cloud optical/microphysical products and their impact on radiative forcing simulations, *Ieee Transactions On Geoscience And Remote Sensing*, *45*(9), 2886–2899.

Zinner, T., and B. Mayer (2006), Remote sensing of stratocumulus clouds: Uncertainty and biases due to inhomogeneity, *J. Geophys. Res.*, *111*(D14209), doi:10.1029/2005JD006,955.

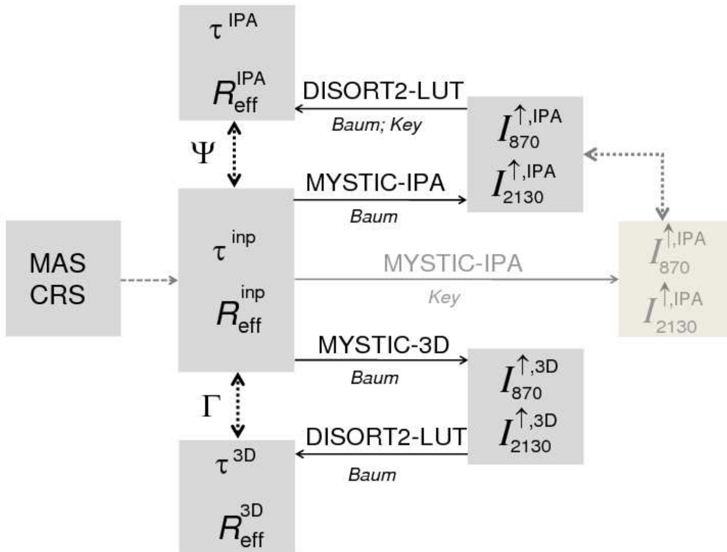

Figure 1. Schematic of the methodology applied in this study. In the first step, a 3D cloud field (τ^{inp} and $R_{\mathrm{eff}}^{\mathrm{inp}}$) is generated from MAS and CRS data. Next, radiative transfer calculations are made with the MYSTIC code using the same Baum ice cloud models (*Baum-mix*) taken in the MODIS/MAS cloud product algorithm: both the 3D (MYSTIC-3D), and independent pixel approximation modes (MYSTIC-IPA) are run. The resulting fields of upwelling radiance $I_\lambda^\uparrow$ (cloud top reflectance r) at two wavelengths (870 nm and 2130 nm) are used to retrieve back the optical thickness and effective radius using pre-calculated lookup tables (LUT) of reflectance pairs generated with DISORT2. The retrieved values for τ^{3D} and $R_{\mathrm{eff}}^{\mathrm{3D}}$ based on $I_\lambda^{\uparrow,\mathrm{3D}}$ (using the *Baum-mix*-LUT) are compared with the original input values, and their pixel-by-pixel ratio Γ serves as a measure for 3D-effects. From the MYSTIC-IPA based radiance fields, values for τ and R_{eff} are retrieved back using LUTs with various sets of single scattering properties (*Key-plt*, *Key-scl*, *Key-agg*, see text for details), and the pixel-by-pixel ratio of the retrieved values to the original values Ψ serves as a measure for ice crystal habit effects. Additionally (shaded in grey), upwelling radiances $I_\lambda^\uparrow$ determined with MYSTIC-IPA (*Baum-mix*) are compared to MYSTIC-IPA (*Key-plt*, *Key-scl*, *Key-agg*) to single out the crystal shape effect on $I_\lambda^\uparrow$.

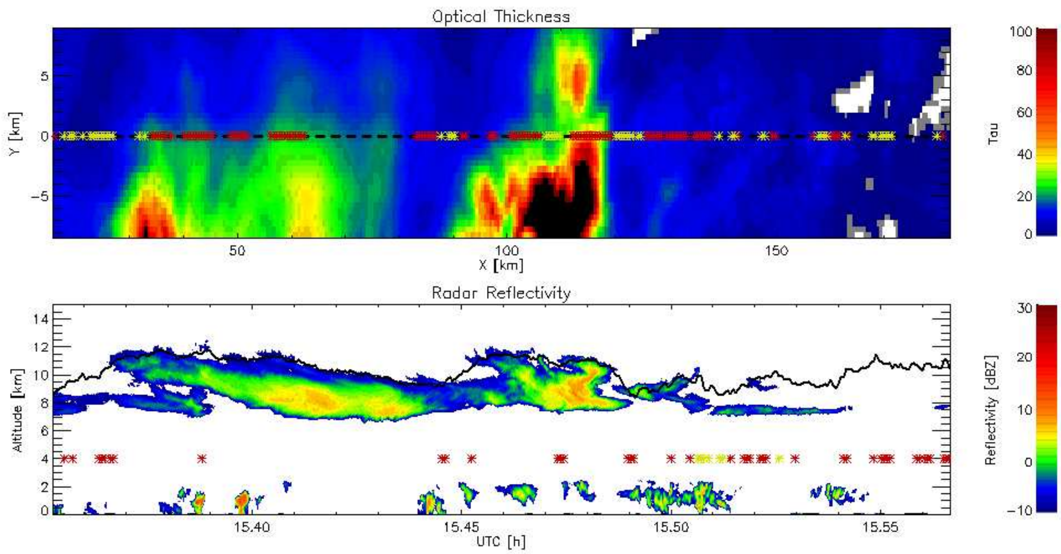

Figure 2. Cloud data from the ER-2 for a portion of the 17 July 2007 flight track (15:21 to 15:34 UTC) used in generating the 3D cloud. Upper panel: MAS-retrieved cloud optical thickness τ (swath 17.5 km) gridded to 500 m resolution. Clear-sky gaps are represented in white. Crosses at y = 0 km (ER-2 flight track) indicate regions at which τ retrieved with 3D calculations was under-/ overestimated (dark red/yellow). Lower panel: Radar reflectivity from CRS in dBZ with cloud top height from MAS along the ER-2 flight track (thick black line). Crosses indicate regions at which R_{eff} retrieved with 3D calculations was under-/ overestimated (dark red/yellow). The marks are explained in Secion 3.1.

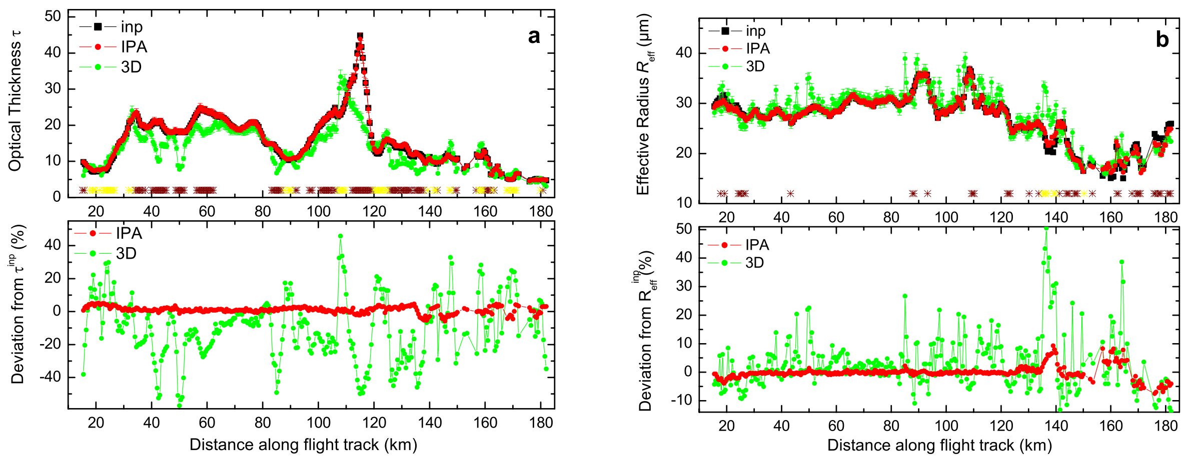

Figure 3. Comparison of the input cloud τ^{inp} (left panel, (a)) and $R_{\mathrm{eff}}^{\mathrm{inp}}$ (right panel, (b)) with retrieval results along nadir track of the ER-2. MYSTIC-IPA (red) and MYSTIC-3D (green) results using the *Baum-mix* single scattering properties are shown. In the upper panels, regions where 3D results under-/overestimated input cloud values are marked with dark red/yellow crosses. In the bottom panel, relative deviations of the IPA- and 3D- based retrieval results from the input cloud values are plotted.

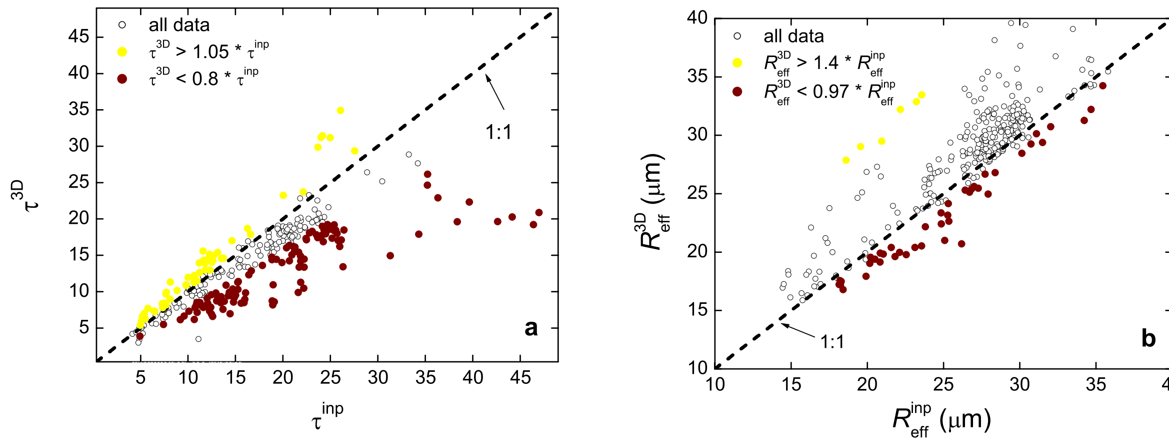

Figure 4. Retrieved τ^{3D} versus τ^{inp} (left panel, (a)) and R_{eff}^{3D} versus R_{eff}^{inp} (right panel, (b)) assuming *Baum-mix*. Under- and (strong) overestimation of input cloud values are marked with dark red and yellow symbols, respectively.

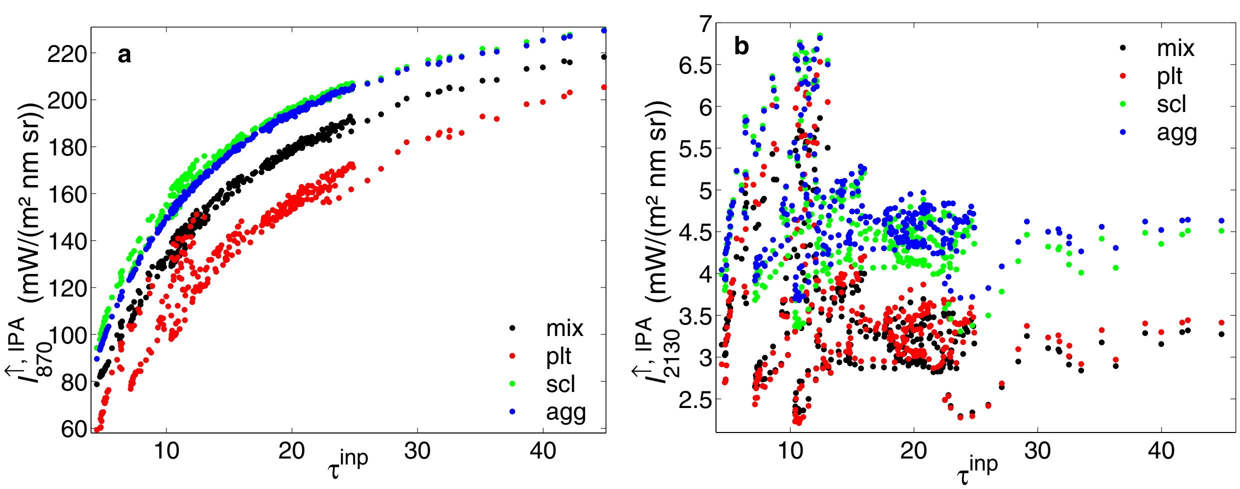

Figure 5. (a) $I_{870}^{\uparrow,\mathrm{IPA}}$ versus τ^{inp} and (b) $I_{2130}^{\uparrow,\mathrm{IPA}}$ versus τ^{inp}. Mix refers to *Baum-mix*, plt to *Key-plt*, scl to *Key-scl*, agg to *Key-agg*.

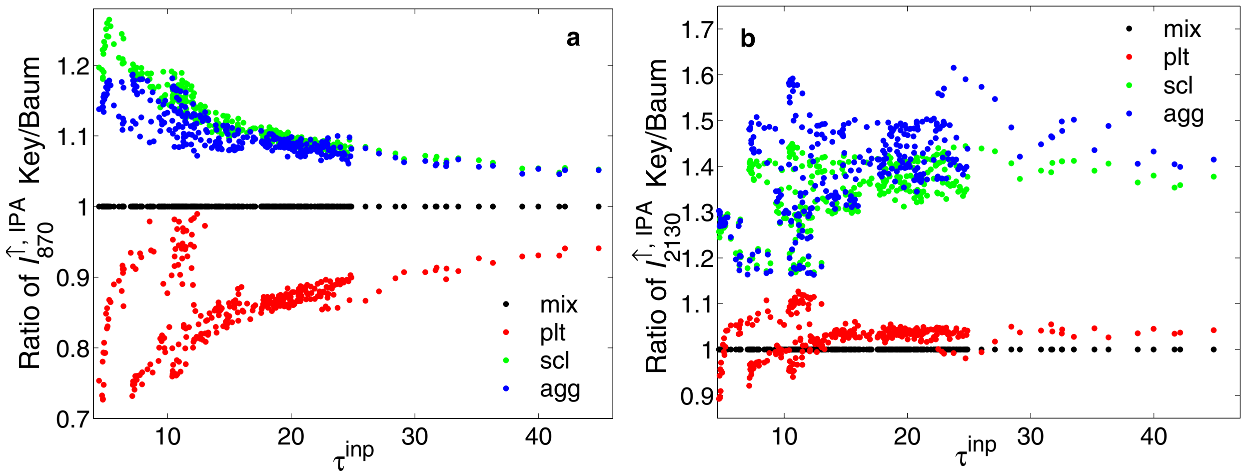

Figure 6. (a) Ratio of $I_{870}^{\uparrow,\mathrm{IPA}}$(Key) to $I_{870}^{\uparrow,\mathrm{IPA}}$(*Baum-mix*) versus τ^{inp}. (b) Ratio of $I_{2130}^{\uparrow,\mathrm{IPA}}$(Key) to $I_{2130}^{\uparrow,\mathrm{IPA}}$(*Baum-mix*) versus τ^{inp}. Mix refers to *Baum-mix*, plt to *Key-plt*, scl to *Key-scl*, agg to *Key-agg*.

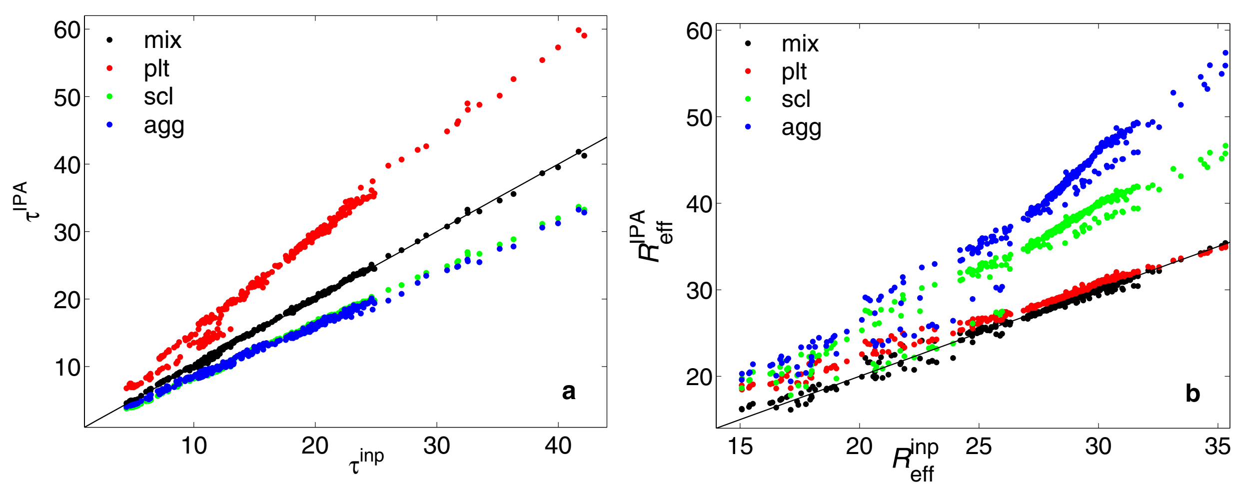

Figure 7. (a) Retrieved τ^{IPA} versus τ^{inp} and (b) $R_{\mathrm{eff}}^{\mathrm{IPA}}$ versus $R_{\mathrm{eff}}^{\mathrm{inp}}$. Mix refers to *Baum-mix*, plt to *Key-plt*, scl to *Key-scl*, agg to *Key-agg*.

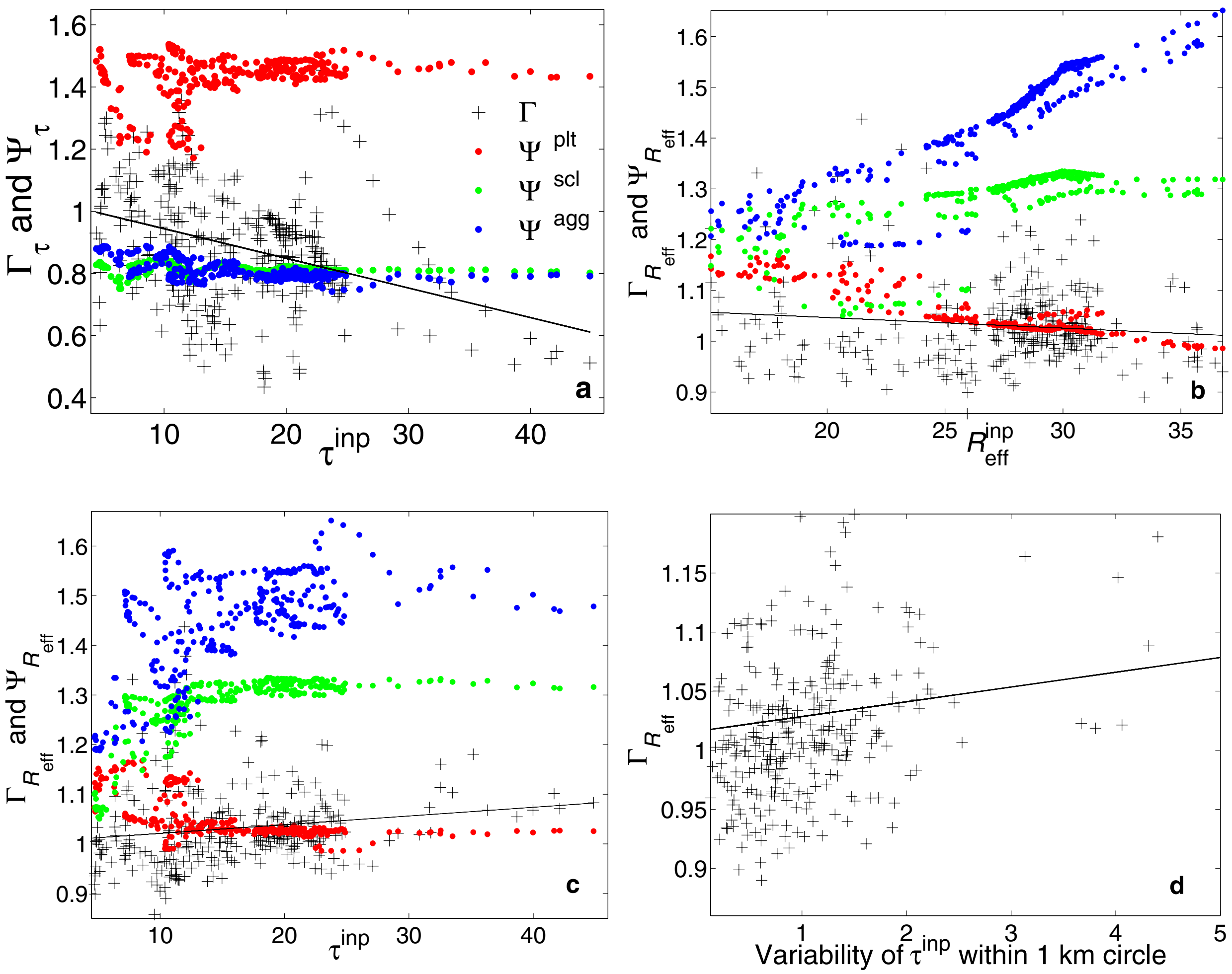

Figure 8. (a) Γ_τ and Ψ_τ versus τ^{inp}. (b) $\Gamma_{R_{\mathrm{eff}}}$ and $\Psi_{R_{\mathrm{eff}}}$ versus $R_{\mathrm{eff}}^{\mathrm{inp}}$. (c) $\Gamma_{R_{\mathrm{eff}}}$ and $\Psi_{R_{\mathrm{eff}}}$ versus τ^{inp}. (d) $\Gamma_{R_{\mathrm{eff}}}$ versus variability of τ^{inp} within a circle of 1 km radius. In (a)-(d), Γ is indicated by black crosses, linear fits of Γ are shown by the black line, Ψ^{plt}, Ψ^{scl}, Ψ^{agg} refer to *Key-plt*, *Key-scl*,*Key-agg*, respectively.